INORGANIC CHEMISTRY
FRONTIERS

RESEARCH ARTICLE

View Article Online
View Journal | View Issue

Cite this: *Inorg. Chem. Front.*, 2024, **11**, 4229

A sunlight sensitive metal–organic framework film for the environment-friendly self-sterilization application†

Lingwan Hao,[a] Jie Gao,[b] Xiaoli Han,[a] Zexiang Li,[a] Yanhong Dong,*[a] Liwei Sun,[a] Lu Zhou,[a] Zhaocai Ning,[a] Jie Zhao [b] and Rujian Jiang *[a]

Frequent outbreaks of respiratory diseases caused by the spread of pathogenic microorganisms poses a great threat to human health. Disposable surgical masks (SM) can limit the transmission to some extent but the inability to self-sterilize leads to a potential source of cross-contamination as well as causing hazardous impacts on the soil and aquatic ecosystems. Herein, a sunlight-triggered photoactive self-sterilization metal–organic framework (MOF) film modified SM is reported. The MOF film can be prepared easily and quickly by the co-assembly of UiO-66 nanoparticles and metal-phenolic networks (MPNs, the complexation of tannic acid and iron ions). Unlike the traditional MPN only assisted assembly, this MOF film exhibited a dramatic synergetic photodynamic and photothermal self-sterilization ability for protective equipment surfaces under simulated-solar irradiation without any extra photosensitizers or photothermal agents. A study of the mechanism revealed that the light absorption region of UiO-66 can be expanded by the MPNs, demonstrating a unique photocatalytic sensitization, and thus the MOF film can utilize the sunlight extensively to achieve a photodynamic property. Moreover, such an MOF film demonstrated excellent cytocompatibility, haemocompatibility and breathability, indicating the security of the skin-touched application. This dual-modal photocatalytic MOF film are promising for the long-term usage of disposable protective equipment and for mitigating the heavy burden on the environment.

Received 22nd March 2024,
Accepted 23rd May 2024

DOI: 10.1039/d4qi00715h

rsc.li/frontiers-inorganic

Introduction

Severe respiratory diseases, caused by various kinds of pathogenic microorganisms (including viruses, bacteria, and fungi), have posed long-lasting severe threats to both personal health and public safety, as witnessed by the spread of "Spanish flu", "A/H1N1 influenza", "mycoplasma infections" and the ongoing global pandemic of COVID-19 variants.[1–4] Generally, the spread of infectious microorganisms is due to direct inhalation of hazardous bioaerosols and emitted droplets, as well as the physical contact with surfaces where aerosols and droplets are present.[5,6] Although vaccinations can reduce the probability of infection in vaccinated people or protect them from suffering severe symptoms, the fast emergence of new variants will gradually weaken its effects, and the worse condition is that there is still lack of effective vaccines for the inhibition of most pathogenic microorganism related respiratory diseases.[7] In this context, daily mask-wearing, which could provide a physical filtration barrier to curb and intercept the continuous transmission of these hazardous airborne microorganisms, has been recognized as a priority.[8] However, the global enforcement of mask-wearing has led to billions of single-use N95 surgical masks being discarded daily, which caused a significant burden on the environment.[9] Additionally, commercial masks can only act as a passive physical barrier and have no function to inactivate pathogens accumulated on their surfaces, which may cause serious secondary contamination and even increase the potential risks of infection to the wearer.[10] Thus, replacing the worn masks regularly is of great importance, yet, this would in turn aggravate the waste of masks.[11] Therefore, given this high risk of secondary contamination and environmental impact, it is urgent to explore a next-generation mask with broad-spectrum inactivation and which is easy to sterilize for reusable and long-term usage.

Photo-activated biocidal strategies, which could utilize photosensitizers (PS) to generate reactive oxygen species (ROS) or overheating upon irradiation to inactivate pathogenic microorganisms, have recently emerged as promising approaches for

[a]*School of Chemistry and Pharmaceutical Engineering, Medical Science and Technology Innovation Center, Shandong First Medical University & Shandong Academy of Medical Sciences, Jinan 250021, China.*
E-mail: jiangrujian@sdfmu.edu.cn
[b]*Key Laboratory of Bionic Engineering, Ministry of Education, Jilin University, Changchun 130022, China*

†Electronic supplementary information (ESI) available: SEM images, DLS measurement image, XRD pattern, XPS spectra, and N_2 adsorption–desorption isotherms. See DOI: https://doi.org/10.1039/d4qi00715h

antimicrobial applications benefiting from the broad-spectrum sterilization capability and satisfactory biocompatibility.[12–14] Several PS materials including inorganic metal oxides (such as TiO_2 and ZnO)[15] as well as organic compounds (such as methylene blue and cyanine dyes)[16] have been introduced into mask systems to improve their self-sterilization efficiency. However, the semiconducting metal oxide PS candidates, that can generate extremely reactive ROS to perform good air disinfection, would usually require UV or blue light for excitation.[17] The chemical conjugation of organic PS compounds into the nanofibers of masks usually require either complex processing or their disinfection efficiency is far from satisfactory due to the organic chemicals and solvent limitation.[18–20]

Alternatively, metal–organic frameworks (MOFs), which are crystalline materials assembled by metal ions with organic struts, have been vigorously investigated in the field of electro- and photo-catalysis.[21] The large specific surface area, high porosity, and tunable post-modification enable MOFs not only to be good candidates for optimizing the photocatalytic performance but also to be an ideal platform for preparing the smart antimicrobial systems upon light irradiation.[22] Currently, most of the MOF materials adopted have been utilized in the form of bulk or powder due to the poor interactions between the raw MOF particles and substrates, which greatly limits their additional applications. Recently, we and other researchers have embarked on studying the fabrication of functionalized MOF films on substrates *via* feasible and scalable methods. In a previous study, we firstly reported that the zirconium-based MOF particle, UiO-66, could generate a suitable amount of ROS under visible light to promote the polymerization of dopamine, which interestingly could assist the UiO-66 film formation on various substrates.[23] By introducing rose bengal into the MOF film, the photosensitizer-adsorbed UiO-66 film demonstrated high-efficiency sterilization under visible light irradiation. Nevertheless, the valid antibacterial period of this method highly relied on maintaining the amount of photosensitizer, which was unsatisfactory for long-term sterilization.

Herein, we present a simple but efficient photoactive Fe@UiO-66@TA/SM film for the self-sterilization of masks. The interaction between ferric ions (Fe^{3+}) and tannic acids (TA, a natural polyphenol) prompted the direct UiO-66 assembly onto the outermost layers of the SM. In particular, it was a notable discovery that the light absorption region of UiO-66 was expanded by the metal-phenolic networks (MPNs), in return, featuring a photothermal and photodynamic antibacterial ability under simulated-solar irradiation without extra PS molecules. Specifically, after irradiation for 20 min, the Fe@UiO-66@TA/SM film showed remarkable antibacterial activity against both Gram-positive bacteria *Staphylococcus aureus* (*S. aureus*) and Gram-negative bacteria *Pseudomonas aeruginosa* (*P. aeruginosa*). Notably, the photocatalysis-functional films displayed prominent prevention and sterilization of the biofilm. Moreover, the Fe@UiO-66@TA/SM film demonstrated excellent breathability, hemocompatibility and cytocompatibility, indicating the security of the skin-touched application. The MPN-assisted UiO-66 assembled antibacterial system described here presents a general strategy for the construction of self-sterilizing SMs with efficient bactericidal properties and high biosafety.

Experimental

Materials

Zirconium(IV) chloride ($ZrCl_4$, ≥99.9%) and tannic acid (TA, ≥99.0%) were purchased from the Aladdin Industrial Corporation. *p*-Phthalic acid (1,4-benzenedicarboxylic acid, H_2BDC, ≥99.0%) and ferric trichloride hexahydrate ($FeCl_3{\cdot}6H_2O$, ≥99.0%) were purchased from Sinopharm Chemical Reagent (Shanghai, China). Tris(hydroxymethyl)aminomethane (Tris, ≥99.9%), sodium sulfate anhydrous (Na_2SO_4, ≥99.95%), and Nafion 117 solution were purchased from Macklin Reagent Company (Shanghai, China). Gram-positive *S. aureus*, *ATCC 6538* and Gram-negative *P. aeruginosa*, *ATCC 9027* were provided by Nanjing Norman Biological Technology Co. Ltd. Luria–Bertani (LB) broth and phosphate-buffered saline (PBS; pH = 7.2 ± 0.2) were purchased from Wuhan Sewell Biological Technology Co., Ltd (China). The L929 cells (mouse fibroblasts) were purchased from BeNa culture collection (BNCC, Suzhou, China). A LIVE/DEAD BacLight bacterial viability kit (L-7012) was obtained from Molecular Probes, Inc. The calcein acetoxymethyl ester (calcein-AM) and propidium iodide (PI) were purchased from Beyotime (Shanghai, China). The CCK-8 (cell counting kit-8) was purchased from Yeasen Biotechnology Co., Ltd (Shanghai, China). Surgical masks (SM) were purchased from Cofoe Medical Technology Co., Ltd (Hunan, China).

Preparation of the UiO-66 particles

The UiO-66 nanoparticles were prepared according to a method in the literature with slight adjustments.[24] The $ZrCl_4$ (53 mg, 0.227 mmol), H_2BDC (34 mg, 0.227 mmol), and acetic acid (450 μL) were fully dissolved in dimethylformamide (DMF, 15 mL) under ultrasonic mixing. The mixture obtained was sealed in a Teflon-lined stainless-steel autoclave and placed in an oven at 120 °C for 24 h. After slow cooling to room temperature, the products were centrifuged and washed three times with DMF and methanol. Then white UiO-66 crystals were obtained after vacuum-drying at 60 °C for 24 h.

Preparation of the Fe@UiO-66@TA

The Fe@UiO-66@TA films and particles were synthesized using a typical one-pot method. The outermost layers of the SM were chosen as model substrates. Before modification, the substrates were cleaned by sonication with ethanal and ultrapure water for 20 min. After vacuum-drying, the SM films were cut into 2 × 1.5 cm^2 sized pieces.

Fe@UiO-66@TA films. The assembly solution was prepared by dispersing $FeCl_3{\cdot}6H_2O$ (1.6 mg mL^{-1}), TA (3.2 mg mL^{-1}), and UiO-66 (2 mg mL^{-1}) separately into the Tri-HCl buffer

solution (pH = 8.5, 10 mmol L^{-1}). Additionally, the UiO-66 nanoparticles and TA were simultaneously dispersed in the assembly procedure. The assembly sequence was as follows: the SM were immersed into the $FeCl_3 \cdot 6H_2O$ solution for 5 min, followed by the addition of the TA solution (5 mL) or the TA solution containing UiO-66 (5 mL). The mixture would turn to dark blue rapidly and was then shaken for another 5 min. This assembly cycle was repeated 10 times. The samples obtained were rinsed in ultrapure water and dried at 60 °C in an oven, which were designated as Fe@TA/SM Fe@UiO-66@TA/SM.

Fe@UiO-66@TA particles. Like the preparation of the Fe@UiO-66@TA films, the assembly sequence was repeated 10 times without the addition of substrates. The Fe@TA and Fe@UiO-66@TA particles were centrifuged from the resulting solutions and dried at 80 °C in an oven.

Electrochemical measurement of the Fe@UiO-66@TA

The Mott–Schottky (MS) analysis was carried out on a CHI760E electrochemical workstation (CH Instruments, China) in a standard three electrode system with the counter electrode and reference electrode (Pt foil, Ag/AgCl in 3 mol L^{-1} KCl). The Na_2SO_4 (0.5 mol L^{-1}) was used as an electrolyte. Nanoparticles (10 mg) were dispersed in the Nafion solution (500 μL, 0.5%) by sonication. Then the homogeneous ink solution obtained was dropped evenly and dried on the surface of the ITO glassy electrode. The MS measurements were carried out in the frequency range of 1000 Hz to 1500 Hz with a 10 mV perturbation.

The band gaps of UiO-66 and Fe@UiO-66@TA particles were calculated according to the following formula:

$$\alpha h\nu = A(h\nu - E_g)^{n/2} \quad (1)$$

where α is the optical absorption coefficient, h is the Planck constant, ν is the optical frequency, E_g is the band gap energy, and A is a constant (mainly the UV-vis DRS absorbance). Additionally, n is related to the optical transition types of the semiconductor, where the direct allowed transition is 1 and the indirect forbidden transition is 4.[25,26] Therefore, UiO-66 is a typical direct semiconductor material (n = 1).[27]

Photothermal conversion measurement

The photothermal conversion effects of the SM, Fe@TA/SM, and Fe@UiO-66@TA/SM samples were measured by simulating the solar illumination. During the simulation, the temperature of each sample was recorded at 5 s intervals for a total of 180 s using a thermal imager (FLIR E5-XT). To evaluate the photostability of the Fe@UiO-66@TA/SM, the sample was exposed to on/off cyclic irradiation for 180 s followed by cooling to room temperature. The irradiation cycle was repeated five times. Moreover, to avoid the experimental error that might be caused by the high power of the simulated-solar light itself, diffusion heat treatment was used throughout the whole test.

In vitro antibacterial tests

S. aureus and *P. aeruginosa* were chosen as the representative Gram-positive and Gram-negative bacteria, respectively. Prior to the tests, all the experimental materials were sterilized in an autoclave, and samples (SM, Fe@TA/SM, and Fe@UiO-66@TA/SM) were placed in 12-well plates followed by UV sterilization for 30 min. The Luria–Bertani (LB) broth bacterial suspension (10^6 CFU per mL, 3 mL) was added to the plates and they were cultured in a 37 °C oven for 3 h. After incubation, the samples were moved to a new plate followed by irradiation with the simulated-solar illumination for 20 min. In addition, to avoid the experimental error that might be caused by the high power of the light, the diffusion heat treatment was used throughout the whole illumination progress, and the simulated-solar light was 40 cm above the samples. As a reference, all the corresponding samples were kept in darkness for 20 min. Then, 3 mL of PBS buffer was added to the plate and mixed ultrasonically for 3 min. Next, 100 μL of the resultant bacterial suspension was placed onto the LB-agar culture medium plates and evenly spread. Subsequently, the Petri dishes were incubated in a 37 °C oven for 16 h, photographed, and then the bacteria colonies were counted.

In vitro anti-biofilm tests

The *P. aeruginosa* was chosen as the representative bacteria to evaluate the anti-biofilm property. Prior to the tests, all the experimental materials were sterilized in an autoclave, and PET films were cut into 1.0 × 1.5 cm^2 sized pieces and sterilized by UV light for 30 min. All the samples (SM, Fe@TA/SM, and Fe@UiO-66@TA/SM) were placed in 12-well plates followed by UV sterilization for 30 min. The PBS bacterial suspension (10^7 CFU per mL, 2 mL) was added to the plates and the cells were cultured in a 37 °C oven for 3 h. Then, the samples were taken out, gently washed with PBS, and this was followed by the irradiation with the simulated-solar illumination for 20 min. Afterwards, all the samples were moved to a new 6-well plate and Luria–Bertani (LB) broth was added to each well before a 3 min ultrasound treatment. Then the samples were discarded, and replaced by the pre-cut PET films and incubated for 24 h at 37 °C. The resulting PET pieces were slightly washed with PBS and stained with a LIVE/DEAD BacLight bacterial viability kit for 15 min in the dark. After a freeze-drying procedure, the PET pieces were photographed using confocal laser scanning microscopy (CLSM, Zeiss Celldiscoverer 7, Germany) and then analyzed by ImageJ software to observe the growth of the biofilms.

To test the property of the anti-biofilm, PET pieces were first immersed into LB broth bacterial suspensions (10^7 CFU per mL, 2 mL) to form a biofilm at 37 °C. Afterwards, the obtained PET were covered with samples (SM, Fe@TA/SM, and Fe@UiO-66@TA/SM) and this was followed by 20 min of simulated-solar illumination. The resulting PET pieces were slightly washed with PBS and stained with a LIVE/DEAD BacLight bacterial viability kit for 15 min in the dark. After a freeze-drying procedure, the bacteria on PET pieces were photographed using the confocal laser microscopy (Zeiss Celldiscoverer 7, Germany) and then analyzed by ImageJ software.

In addition, all the corresponding samples were kept in the darkness for 20 min as reference samples. To avoid the experi-

mental error that might be caused by the high power of the light, the diffusion heat treatment was used throughout the whole illumination progress, and the simulated-solar light was placed 40 cm above the samples.

In vitro cytocompatibility assay

The calcein acetoxymethyl ester (calcein-AM) and propidium iodide (PI) dual staining was adopted to observe the cytocompatibility of the samples. Firstly, L929 normal fibroblast cells were seeded into a 48-well plate (10^4 cells per well, 100 μL medium) for 24 h. Then the medium was refreshed and co-cultured with samples for another 24 h. Next, each well was gently washed with PBS and stained with a calcein-AM/PI mixture at 37 °C for 30 min. Then each well was washed three times with PBS, and photographed using the confocal laser microscope (Zeiss Celldiscoverer 7, Germany).

Then, the standard CCK-8 (cell counting kit-8, Kumamoto, Japan) assay was carried out to estimate the cytocompatibility of the samples. Before the test, the samples were immersed into a high glucose Dulbecco's modified Eagle's medium (HG-DMEM) with 10% foetal bovine serum (FBS) and 1% penicillin/streptomycin for 24 h to obtain the soakage solutions. The cells were seeded into a 96-well plate (10^4 cells per well, 100 μL medium) and placed in a 5% CO_2 incubator at 37 °C for 24 h. Afterwards, cell incubation solutions were replaced by the above soakage solution (100 μL per well). After a further 24 h of incubation, the soakage solutions were removed, each well was washed with PBS, followed by the addition of 100 μL of 10% CCK-8 solution. After staining for 1 h in darkness, the absorbance of each well at 450 nm was immediately determined using an enzyme marker. In addition, the control group was performed using the only HG-DMEM solution (with 10% FBS and 1% PS), and all experiments were carried out in triplicate and the results were used to create the statistical data.

In vitro hemocompatibility assay

Fresh rabbit blood was used to determine the hemocompatibility of samples. Prior to the test, all the samples were cut into 0.5 × 0.5 cm^2 pieces and immersed in PBS buffer (pH = 7.2 ± 0.2) at 30 °C for 1 h to equilibrate the surface. The fresh rabbit blood was centrifuged for 15 min (1000 rpm) to separate the platelet-rich plasma (PRP) and the red blood cells (RBC). After removing the supernatant suspension, 2 mL of normal saline was added to dilute and wash the RBC, they were then centrifuged for 5 min (2000 rpm). After washing twice, the RBC solution was diluted to a concentration of 5%. The prepared samples were then put into a 24-well plate, followed by the addition of 300 μL of 5% RBC solution on each surface. After incubation at 37 °C for 2 h, the resulting 5% RBC solution was centrifuged for 3 min (3000 rpm), recorded photographically, and the corresponding OD_{540} values of each supernatant suspension were measured. Additionally, as control experiments, the RBC were diluted in water or normal saline to act as the positive and negative controls, respectively. The haemolysis ratio was calculated according to the following formula:

$$\text{Haemolysis ratio } (\%) = (OD_{sample} - OD_{negative})/(OD_{positive} - OD_{negative}) \quad (2)$$

Breathability tests

The water vapor transmission rates (WVTR) of the samples were measured to evaluate the permeability of the samples.[28] Briefly, samples were cut to a size of 1.5 cm × 1.5 cm and then placed on a vial, which contained 10 mL of ultrapure water. The vial was incubated in an incubator at 37 °C for 24 h and then weighed to calculate the WVTR.

Characterization

The particle and surface morphology were monitored using a scanning electron microscope (SEM, Hitachi, SU8020, Japan) at an accelerating voltage of 5 kV. The internal structures of the samples were characterized by transmission electron microscopy (TEM, Jeol, JEM-2100F). The size distribution and zeta-potentials of all particle samples were determined using dynamic light scattering (Malvern Panalytical, Zetasizer Nano ZS90). The crystal structures of the as-synthesized UiO-66 and modified powders were recorded by X-ray diffraction (XRD, Shimadzu XRD-6000) with Cu-Kα radiation (λ = 1.5418 Å). The chemical composition of the particles and the corresponding surfaces were characterized by Fourier-transform infrared (FTIR, PerkinElmer spectrophotometer) and attenuated total reflectance Fourier-transform infrared spectroscopy (ATR-FTIR, Bruker Vertex 70v). Thermogravimetric analysis (TGA) was conducted on a thermal analyser (Bruker, Vertex 70v) from room temperature to 800 °C under an air atmosphere with a heating rate of 10 °C min^{-1}. The UV-vis diffuse reflectance spectroscopy (DRS) was conducted on an ultraviolet and visible light spectrophotometer (PerkinElmer, Lambda 950). The optical density (OD) values were determined by a Multiskan SkyHigh Microplate Spectrophotometer (ThermoScientific, A51119600).

Results and discussion

Assembly and characterization of the Fe@UiO-66@TA films

The simple and scalable preparation for producing Fe@UiO-66@TA film is shown schematically in Fig. 1. The UiO-66 particles were first prepared according to a previously reported hydrothermal reaction method.[24] As shown in Fig. 1a, the as-synthesized UiO-66 particles were mostly uniform, smooth, and intact. Corresponding to the scanning electron microscopy (SEM) image, the dynamic light scattering (DLS) result showed that the UiO-66 particles were mainly monodispersed with a diameter of ~305 nm (Fig. 1b). A vital measurement of MOF crystal composition, X-ray diffraction (XRD), was used to further determine the crystal formation of the UiO-66. As shown in Fig. 1c, the characteristic peaks of the as-prepared

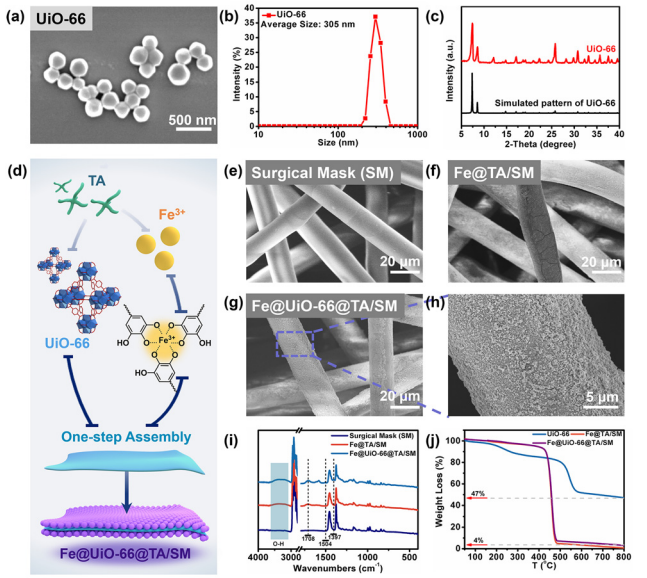

Fig. 1 (a) The SEM image, (b) the DLS measurement image, and (c) the XRD pattern of the UiO-66 particles, (d) the Fe@TA LbL assembly of the UiO-66 particles, the SEM images of (e) a pristine SM, (f) the Fe@TA/SM, and (g and h) Fe@UiO-66@TA/SM. (i) The ATR-FTIR and (j) TGA curves of Fe@TA/SM and Fe@UiO-66@TA/SM films.

particles were in good agreement with the simulated UiO-66 XRD pattern, indicating that the UiO-66 crystal particles with a high purity had been successfully constructed.[29,30] Furthermore, the UiO-66 particles can maintain an intact morphology and crystal structure after being immersed in Tris-HCl buffer (pH = 8.5) for 2 h (Fig. S1†), demonstrating an excellent stability for subsequent assembly processes.

Due to the poor interactions between the raw MOF particles and substrates, it was difficult to prepare uniform MOF films on the material's surface. Mussel inspired, surface-modified techniques have been widely proven to be a simple and rapid strategy for constructing nanofilms on various substrates.[31] In this context, the UiO-66 particles were constructed on the surface of the SM substrate with the assistance of the assembly between tannic acid (TA) and ferric ions (Fe^{3+}), and the resulting film was designated as Fe@UiO-66@TA/SM (Fig. 1d). As shown in Fig. 1e, the pristine SM was composed of crosslinked fibers with a smooth morphology and a dimensional network which leads to high air permeability. A similar appearance was seen on the SM which was treated only with UiO-66 particles, demonstrating that virtually no UiO-66 particles were immobilized on the SM (Fig. 1f). In comparison, some small nanoparticle agglomerations could be observed on the fiber surface which was treated by the TA/Fe solution for only 5 min, confirming their easy and fast assembly capability on substrates (Fig. 1g). As such, when the UiO-66 particles and TA/Fe solution were synchronously added into this system, the nanostructures which may involve the UiO-66 crystal and the TA/Fe assembly were evenly and broadly grown on the surface of the SM fiber, indicating the successful construction of the hybrid coating (Fe@UiO-66@TA) (Fig. 1h). Notably, the dimensional network of the fibers was still maintained even after 10 cycles of co-assembly between the UiO-66 particles and the TA/Fe solution, which guarantees permeability during the wearing of the SM. The elemental analysis (Fe, Zr) of the Fe@UiO-66@TA/SM films by XPS confirmed the loading of UiO-66 and Fe/TA (Fig. S2†).

The attenuated total reflection-Fourier infrared (ATR-FTIR) was employed to investigate the chemical variations of the SM surfaces caused by the co-assembly of UiO-66 and TA/Fe (Fig. 1i). Compared with the pristine SM surface, the remarkable increase of the bands at 3100–3600 cm^{-1} for Fe@TA/SM and Fe@UiO-66@TA/SM were attributed to the O–H stretching of TA.[32] Moreover, the absorption peak at 1708 cm^{-1} belonged to the characteristic band of –COOH in TA, further confirming the existence of the Fe@TA coatings.[33] As displayed in the curve of Fe@UiO-66@TA/SM, two new absorption peaks appeared at 1504 and 1397 cm^{-1}, which were attributed to the ligand of the UiO-66 particles (benzene ring C=C and –COOH vibration) On the basis of the above results, the Fe@UiO-66@TA films were successfully constructed on the surface of the SMs.

The thermal stabilities of the UiO-66, Fe@TA/SM and the Fe@UiO-66@TA/SM films were evaluated by thermo-gravimetric analysis (TGA) (Fig. 1j). For the Fe@TA/SM and Fe@UiO-66@TA/SM films, the loss of the adsorbed water occurred before 200 °C. The sharp weight loss between 450 °C and 475 °C might be ascribed to the degradation of the SM. For the UiO-66 particles, the degradation of the organic frameworks occurred at 550 °C, leaving a residual weight of 47%. The residual weights of UiO66 and Fe@UiO-66@TA/SM were about 47% and 4%, respectively. The amount of the Fe@TA-assisted particles used in the assembly of the Fe@UiO-66@TA/SM films was calculated to be approximately 8.5%.

Verification of the assembled Fe@UiO-66@TA nanoparticles

As demonstrated, with the help of the unique complexation between polyphenol and iron, the UiO-66 particles could be readily assembled onto the fiber of the SMs. To further investigate the assembly process and mechanisms, the nanoparticles produced in the mixed solution were collected and analysed (Fig. 2a). As shown in Fig. 2b, compared with the smooth and conformal surface of the pristine UiO-66 (Fig. 1a), the Fe@UiO-66@TA particles were evenly covered by the spot-like rougher surface morphology. Furthermore, the DLS analysis was utilized to verify the size change of the Fe@UiO-66@TA particles. After modification, the diameter of the particles increased to ~326 nm, demonstrating that nano-films were formed on the UiO-66 surfaces (Fig. 2c). Additionally, the transmission electron microscopy (TEM) image of the hybrid Fe@UiO-66@TA particles exhibited a typical core–shell structure, further confirming that the UiO-66 particle was enfolded in an MPN coating (Fig. 2d). The TEM and the EDS-mapping of the Fe@UiO-66@TA nanoparticles for the C, Fe, O, and Zr elements (Fig. 2e) was carried out, and demonstrated the suc-

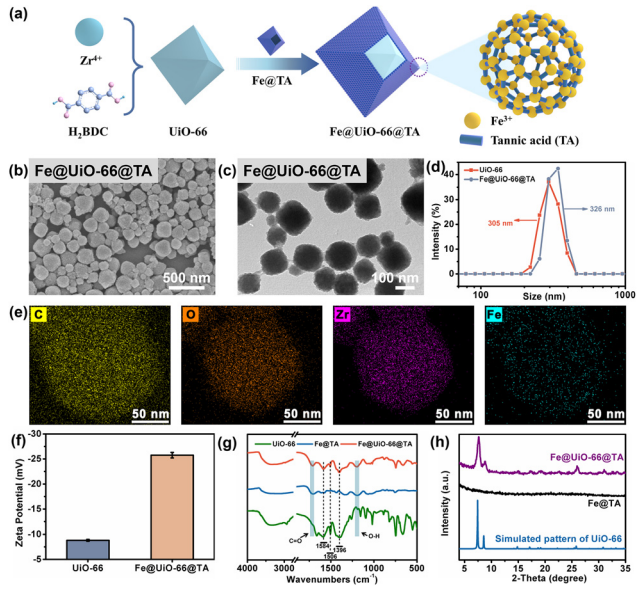

Fig. 2 (a) Schematic illustration of the one-pot modification of the particles. (b) An SEM image and (c) a TEM image, and (d) the DLS measurement graph of the Fe@UiO-66@TA particles. (e) The elemental mappings of Fe@UiO-66@TA for the distribution of the C (yellow), O (orange), Zr (pink) and Fe (light blue) elements, (f) the graph of the zeta-potentials of UiO-66 and Fe@UiO-66@TA particles, (g) the FTIR scans of the UiO-66, Fe@TA, and Fe@UiO-66@TA particles, and (h) the XRD patterns of the Fe@TA and Fe@UiO-66@TA particles.

cessfully assembly of the MPN on the UiO-66 surface, guaranteed the subsequent synergetic PTT and PDT effects.

To confirm that the outermost coating of the UiO-66 particle came from the Fe@TA complex, the property of the Fe@UiO-66@TA particles were characterized using zeta-potentials and the FTIR spectrum. Compared with the pristine UiO-66 particles, the zeta-potential of Fe@UiO-66@TA showed decreased values which may be attributed to the increased hydroxyl groups originating from TA, and thus demonstrating the existence of TA on the particle surfaces (Fig. 2f). As further revealed by the FTIR spectrum, when compared with pristine UiO-66, the Fe@UiO-66@TA hybrid nanoparticles exhibited new absorbance bands at 1584 cm^{-1} and 1396 cm^{-1}, which belonged to the asymmetric and symmetric stretching of carboxyl functional groups (O=C–OH), respectively (Fig. 2g). Additionally, the characterization peak of 1506 cm^{-1} was attributed to the C=C in the benzene rings.[23,34] Moreover, the Fe@UiO-66@TA, when compared with the Fe@TA, displayed intensive absorbance bands at 1710 cm^{-1} and 1194 cm^{-1}, and these corresponded to the vibrations of the C=O and O–H in TA, respectively.[35] The above characterization peaks revealed that the outermost coating on the surface of the UiO-66 particle was the Fe/TA complex.[36] Collectively, these results demonstrated that the co-assembly of UiO-66 and Fe/TA on the SM fibers might start from the decoration of the Fe/TA complex for UiO-66, and subsequently formed the Fe@UiO-66@TA particles integrally adhered onto the fiber surface. Accordingly, this phenomenon demonstrated a feasible and convenient strategy to prepare MOF thin films on the desired substrates, which may help to expand the applications of functionalized MOFs.

To investigate whether the performances of the UiO-66 particles was compromised after the introduction of the Fe/TA coating on their surfaces, the BET surface area and porosity property of the particles were first evaluated using the N_2 adsorption–desorption isotherms. As shown in the Fig. S3 and Table S1,† the BET surface area of the Fe@UiO-66@TA (128.2 ± 3.1 m^2 g^{-1}) was decreased when compared with the pristine UiO-66 particles (957.8 ± 27.8 m^2 g^{-1}), indicating that the layer-by-layer (lbl) assembly of the non-porous Fe@TA could brought impact on the porosity property when endowing the excellent PTT/PDT property of pristine UiO-66. Moreover, the Fe@UiO-66@TA hybrid nanoparticle displayed the same typical XRD patterns as the pristine UiO-66 particles (Fig. 2h), demonstrating that the physical crystalline structures of UiO-66 could be maintained well, even after the introduction of the Fe/TA coating. Therefore, the Fe/TA coating caused no damage to the UiO-66 particles.[37]

Photocatalytic sensibilization and photothermal property of the Fe@UiO-66@TA

Taking advantages of the fast assembly property and excellent photothermal effect, the TA/Fe nanoparticles or coatings have been used intensively to combat bacterial infections.[38] Generally, a satisfactory photothermal therapy (PTT) would require prolonged and hyperthermic (above 70 °C) treatments, however, the hyperthermia effect would inevitably lead to severe side effects for patients.[39] As an alternative, the synergism of photodynamic therapy (PDT) and PTT could achieve superior antibacterial performances under moderate temperatures and biocompatible conditions. However, the realization of the synergistic therapy promises a co-irradiation treatment with different wavelengths, which creates a complicated and tedious procedure.[22] In previous work, we first reported that UiO-66, a classical Zr-based MOF with high structural stability and excellent biocompatibility, could generate a small but suitable amount of reactive oxygen species (ROS) under visible light with the assistance of the dopamine-sensitized effect.[23] Therefore, in addition to the PTT effect from the Fe@TA, we speculated that the hybrid Fe@UiO-66@TA might also generate ROS which originated from the sensibilization, which was like using dopamine under a single light source.

To verify this hypothesis, the measurement of the ultraviolet-visible diffuse reflection spectrum (UV-vis DRS) was first used to observe the optical absorption abilities of the Fe@UiO-66@TA particles. As shown in Fig. 3a, the pristine UiO-66 particle had almost no visible light absorption under the irradiation of simulated-solar irradiation. In sharp contrast, after the integration of Fe@TA, the synthesized Fe@UiO-66@TA particles displayed a significant enhanced absorption, demonstrating that the hybrid of Fe@TA on the UiO-66 surfaces effectively extended the visible light adsorption region (Fig. 3d). In addition, to further investigate the optical changes caused by the Fe@TA modification, the band

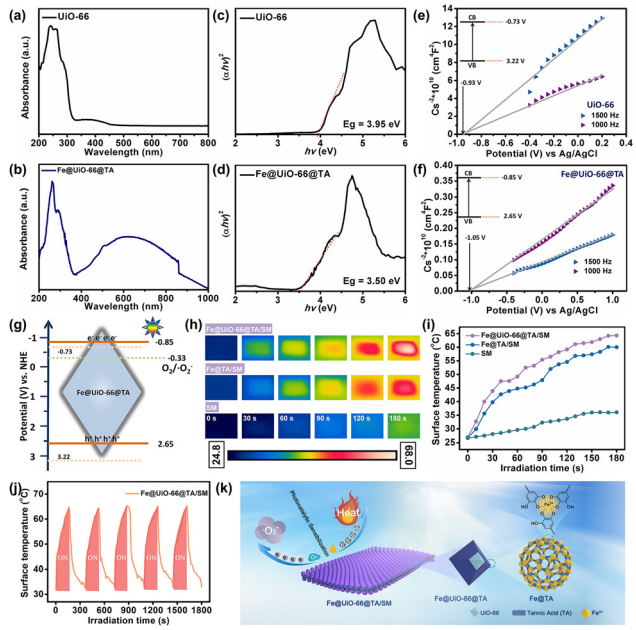

Fig. 3 (a and b) UV-vis diffuse reflectance spectra of UiO-66 and Fe@UiO-66@TA, (c and d) the Tauc plots of UiO-66 and Fe@UiO-66@TA, (e and f) the Mott–Schottky plots for UiO-66 and Fe@UiO-66@TA. (g) The photocatalysis sensibilization of the Fe@UiO-66@TA particles under the simulated-solar irradiation. (h) Photographs and infrared thermal images of SM, Fe@TA/SM and Fe@UiO-66@TA/SM before and after the simulated-solar irradiation for 180 s. (i) Temperature variations of SM, Fe@TA/SM and Fe@UiO-66@TA/SM with the simulated-solar irradiation recording by the infrared camera every 10 s interval. (j) Temperature rising and cooling profiles of when the irradiation is on/off under the simulated-solar irradiation. (k) Schematic illustration of the photocatalytic sensibilization and photothermal property of the Fe@UiO-66@TA.

gap energies (E_g) of the particles were predicted from the Tauc plots. In Fig. 3b, the E_g of the UiO-66 particle was about 3.95 eV, which agreed with the previously reported results.[40] For the Fe@UiO-66@TA, the E_g decreased to 3.50 eV, implying that the Fe@TA coating could narrow the band gap of UiO-66, and thus enhance the potential ability to utilize the visible light region in sunlight (Fig. 3e).

As a further identification of the Fe@TA sensibilization, the valence band potentials (V_{VB}) of the samples were determined using the Mott–Schottky (M–S) spectra at different frequencies to further confirm the Fe@TA catalysis of UiO-66. As illustrated in Fig. 3c and f, after the plot fitting process, both the UiO-66 and Fe@UiO-66@TA exhibited positive slopes, indicating the typical n-type nature of the semiconducting material.[41] Given that the flat-band potential (V_{FB}) of the n-type semiconductors gave the information about the conduction band edge, the V_{FB} values were then estimated.[42,43] The V_{FB} of the samples were calculated from the intersections of the fitted UiO-66 curves and the Fe@UiO-66@TA curves, and the V_{FB} were −0.93 V *vs.* Ag/AgCl and −1.05 V *vs.* Ag/AgCl, respectively. Therefore, the conduction band edges (V_{CB}) of UiO-66 and Fe@UiO-66@TA were about −0.73 V *vs.* NHE and −0.85 V *vs.* NHE, respectively. Combined with the E_g calculated from the UV-vis DRS spectra and the formula, the valence band potentials of UiO-66 and Fe@UiO-66@TA were 3.22 V and 2.65 V. Consequently, the Fe@UiO-66@TA exhibited narrower band gaps and more negative conduction band potentials than the single UiO-66, which was negative enough to reduce the surface adsorbed O_2 to $^{\bullet}O_2^-$ (−0.33 V *vs.* NHE) (Fig. 3g).[44,45] Similarly, the Fe@UiO-66@TA/SM film was expected to be endowed with a unique photocatalytic sensibilization, utilizing sunlight extensively to achieve the photodynamic antibacterial property (Fig. 3f).

In addition, the photothermal effect of the Fe@UiO-66@TA was mediated by Fe@TA, which is known for its mild and bionic PTT performance.[46] The photothermal performances of the samples were firstly evaluated by monitoring the temperature change under the simulated-solar irradiation. As shown in Fig. 3h, the pristine SM presented a slow and insignificant increase in temperature with the extension of the irradiation time, indicating the lack of photothermal conversion of the facemask fibers. In comparison, after the introduction of the Fe@TA complex, rapid and remarkable temperature increases were observed on the hybrid Fe@TA/SM sample, demonstrating that the Fe@TA coating could render the SM with an excellent light-to-heat conversion capability. Notably, with the further integration of UiO-66 into the hybrid SM, the Fe@UiO-66@TA/SM sample showed a more significant increase in temperature (64.5 °C) under the same irradiation conditions (Fig. 3i). This phenomenon might be attributed to the fact that the introduction of the UiO-66 particles increased the content of the metals which accounted for the photothermal conversion. Moreover, the heating/cooling curves were also recorded according to the requirements for the long-lasting stability of the protective equipment. As shown in Fig. 3j, after five cycles, the temperature curve could remain relatively consistent without obvious changes of surface morphology and structure (Fig. S4†). These results collectively suggested that the Fe@UiO-66@TA/SM film could guarantee satisfactory thermal energy under the simulated-solar irradiation.

Antibacterial property of Fe@UiO-66@TA/SM films

Given the ingenious combination of photothermal and photodynamic properties, the *in vitro* antibacterial performance of Fe@UiO-66@TA/SM was evaluated against *S. aureus* and *P. aeruginosa*. To distinguish the individual bactericidal effects between the PDT and PTT, a plate counting method was conducted as in previous research. As shown in Fig. 4a and b, in the absence of irradiation, there was no detectable difference in the bacterial survival rate between Fe@UiO-66@TA/SM and pristine SM, demonstrating that the hybrid Fe@UiO-66@TA had no adverse effects on the bacterial activity. In contrast, a remarkable decrease (80% approximately) of the bacterial survival rates were observed on the Fe@TA/SM for both Gram-positive *S. aureus* and Gram-negative *P. aeruginosa* upon simulated-solar irradiation for only 20 min. This phenomenon indicated that taking advantage of excellent photothermal conversion, the Fe@TA modified substrates could certainly have an

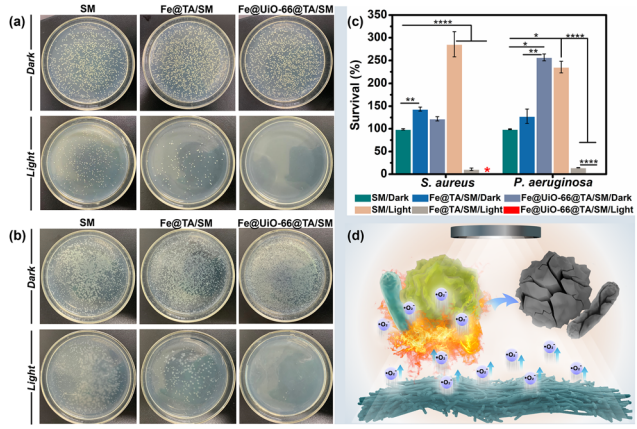

Fig. 4 Representative photographs of the agar plates for (a) *S. aureus* and (b) *P. aeruginosa* on the LB agar plate. (c) The histogram of the relative bacterial survival (%) corresponding to treatments used, and (d) a schematic illustration of the antibacterial properties of Fe@UiO-66@TA/SM films. Significant difference: ****$p < 0.0001$, ***$p < 0.001$, **$p < 0.01$, $p > 0.05$ no significant difference (ns).

encouraging antibacterial capability. However, there was still a non-negligible number of live microorganisms on the Fe@TA/SM surface, which might infect the mask wearer or act as a source of secondary contamination. Notably, under the same irradiation conditions, the SM modified with Fe@UiO-66@TA hybrid nanoparticles displayed a superior bactericidal performance such that there was no detectable bacterial colony observed on the ager plate. Obviously, the extremely high antibacterial efficiency of Fe@UiO-66@TA/SM might be attributed to the synergistic PDT/PTT effect so that the hyperthermia could eliminate most of the adhered bacteria while the outer membrane permeability of the remaining live bacteria was changed simultaneously, which would be convenient for the ROS to have an enhanced bactericidal property (Fig. 4c). These results together revealed that with the Fe@UiO-66@TA nanoparticle, a hybrid photocatalyst, modified surgical mask could be a viable and strong protective strategy against the spread and infection of pathogens (Fig. 4d).

Anti-biofilm property of the Fe@UiO-66@TA/SM film

After the attachment, the microorganisms tend to develop, to form a stubborn biofilm which is not only a suitable microenvironment for bacterial growth but also a protective barrier against biocidal agents. It was verified that up to 1000 times higher tolerance against antibiotics can be achieved by the bacteria embedded in a biofilm when compared to their planktonic counterparts.[47] Therefore, antibacterial surfaces that can prevent the bacterial attachment and restrain the subsequent biofilm formation are highly significant. In this context, we expected that the Fe@UiO-66@TA functionalized surface might have the capability to resist the formation of stubborn biofilms. As a proof-of-concept, the Gram-negative bacteria *P. aeruginosa* was chosen as a model bacterium to assess the prevention and penetration against the biofilm samples because of their continual biofilm formation and tendency to show antimicrobial resistance. Here, two experiments were designed and carried out to test the resistance of the samples to biofilm formation. Briefly, after incubation in the bacterial suspension (PBS, 2 mL, 10^6 CFU per mL) for 3 h, the samples were irradiated under the simulated-solar light or left in the dark for 20 min. Subsequently, the bacterial cells attached onto the pristine or to the particle modified mask surfaces were dispersed in LB media to contaminate the sterile PET which were used as the model substrate to evaluate the recontamination and biofilm formation property of the bacteria. Then, the PET obtained was stained using a LIVE/DEAD BacLight bacterial viability kit (L-7012) and observed under the confocal laser scanning microscope to evaluate the growth of the bacterial cells. As shown in Fig. 5a, after incubation in the LB media, all the PET surfaces processed with the dark group were densely covered with biofilms, indicating that a non-bactericidal surgical mask surface could deliver sufficient live bacteria to perform colonization, proliferation, and biofilm formation on the other fresh substrates. Notably, even when processed with the simulated-solar light irradiation, the contaminated Fe@TA/SM sample could lead to significant biofilm formation on the conceptual PET surface. This result certified that the adhered bacteria could not be completely killed if depending on only the mild photothermal property in this system, and the survival of a small amount of residual bacterial cells could still cause serious biofilms on other sterile

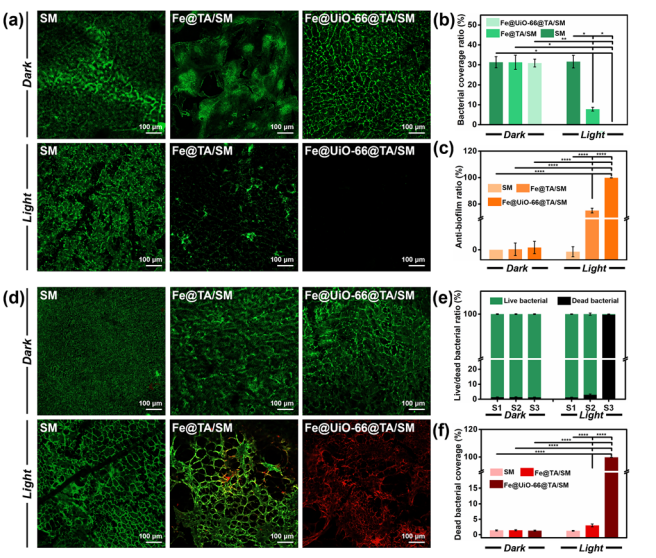

Fig. 5 (a) Representative CLSM images of the *P. aeruginosa* attached to the PET surface obtained for the SM (left), Fe@TA/SM (middle) and Fe@UiO-66@TA/SM (right) solution, (b) a comparison of the bacterial coverage, and (c) anti-biofilm ratio of SM, Fe@TA/SM, Fe@UiO-66@TA/SM samples. (d) Representative CLSM images of *P. aeruginosa* attached on the PET surfaces after treatment with SM (left), Fe@TA/SM (middle) and Fe@UiO-66@TA/SM (right) samples, (e) the corresponding live/dead bacterial coverage statistics, and (f) the dead bacterial coverage of the CLSM images. Significant differences: ****$p < 0.0001$, ***$p < 0.001$, **$p < 0.01$, $p > 0.05$ no significant difference (ns).

surfaces. In sharp contrast, after the same simulated-solar light irradiation for the Fe@UiO-66@TA/SM sample, the extracted suspension was incapable of prompting the bacterial adhesion and biofilm formation on the fresh substrates as verified by the fact that there was no detectable bacterial cells present on the corresponding PET surface. Together these phenomena demonstrated that the as-prepared Fe@UiO-66@TA/SM films take advantage of the synergistic effects of the PDT and PPT and were able to thoroughly sterilize the initial adherent bacteria, and thus they obstructed the biofilm formation and the second contamination for the fresh substrates.

These encouraging results prompted us to investigate whether the Fe@UiO-66@TA modified surfaces could disperse established biofilms. In this experiment, the surgical mask modified with or without the Fe@UiO-66@TA particles were covered by the PET films which had been constructed with mature biofilms in advance, and then the solar-simulated light irradiation was executed for that composite. As shown in Fig. 5d and e, in the absence of simulated-solar light irradiation, numerous activated bacterial cells remained on the PET surfaces treated with pristine SM and Fe@UiO-66@TA/SM. A similar overwhelming green fluorescence of the CLSM image was shown on the SM sample which was suffering from the irradiation of solar-simulated light, indicating that the heat generated by the irradiation within 20 min had negligible effects on the activity of the bacteria embedded in the biofilm. After introducing the Fe@TA nanoparticles onto SM, with the assistance of solar-simulated light irradiation, several patches of red fluorescence (indicating dead bacterial cells) were displayed on the corresponding PET surface. Yet, most of the bacteria covered area (more than 97%) still displayed green fluorescence, indicating that the photothermal effect of the Fe@TA could exert a limited adverse impact for the bacterial activity protected by the biofilm. In contrast, an area covered with a significant number of dead bacteria (more than 99.8%) was observed on the surface treated with Fe@UiO-66@TA/SM and irradiation. Such differences could be attributed to three possible causes: (1) the introduction of the UiO-66 crystals into the hybrid particles could enhance the photothermal effect of the Fe@UiO-66@TA/SM; (2) taking advantage of the photocatalytic sensibilization of Fe@TA complex, the Fe@UiO-66@TA/SM could generate ROS which were harmful for the bacteria; and (3) the photothermal effect could increase the permeability of the biofilm, which rendered the ROS more likely to penetrate the formed biofilms. These results demonstrated that the constructed Fe@UiO-66@TA particle exhibited promising potential for combating preformed biofilms in the presence of solar light irradiation.

In vitro biocompatibility and breathability of the Fe@UiO-66@TA/SM film

As for the biomedical materials, good biocompatibility of the Fe@UiO-66@TA film is essential if direct contact with the skin is being considered. Therefore, the *in vitro* compatibility of

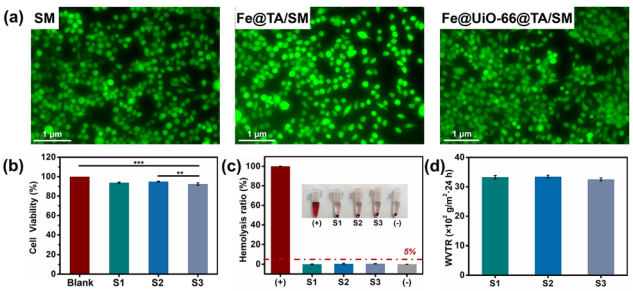

Fig. 6 (a) Representative images of L929 cells cultured with SM, Fe@TA/SM, and Fe@UiO-66@TA/SM, (b) results of the CCK-8 cell viability, (c) the haemolysis ratio (%) and (d) water vapor transmission rate (WVTR) of SM (S1), Fe@TA/SM (S2) and Fe@UiO-66@TA/SM (S3). Inset: digital images of red blood cell suspensions. Significant difference: ****$p < 0.0001$, ***$p < 0.001$, **$p < 0.01$, $p > 0.05$ no significant difference (ns).

Fe@UiO-66@TA/SM was tested using the L929 fibroblast cells and fresh rat blood cells. To evaluate the cytocompatibility of the Fe@UiO-66@TA/SM, a live/dead staining assay was performed to visualize the viability of cells. After a 24 h co-culture with samples, the cells were stained with calcein-AM and PI dual staining dye and observed under a confocal laser microscope. As shown in Fig. 6a, a strong green fluorescence was displayed on the surface, demonstrating that almost no cells were inactivated after incubation with the samples. Moreover, most cells of the Fe@UiO-66@TA/SM group exhibited a typical spindle state of morphology, showing no significant difference when compared to the two other groups. To further quantitatively assess the cytotoxicity of the samples towards the cells, a cell counting kit (CCK-8) test was performed (Fig. 6b). After a 24 h co-incubation with the samples and then staining with a CCK-8 kit, all the cells maintained a viability of more than 92%, demonstrating that the functional film had no adverse influence on the cells.

As another crucial standard of biocompatibility, the haemocompatibility of the samples was then investigated. As shown in Fig. 6c, the haemolysis ratios of the modified surfaces were all less than 5%, which was like the negative control (pure blood cell solution), thus implying a remarkable hemocompatibility. Meanwhile, the water vapor transmission rate (WVTR) of the Fe@UiO-66@TA/SM was found to be 3251 ± 49 g m^{-2} 24 h, which was close to that of the pristine SM (3328 ± 58 g m^{-2} 24 h), indicating that the modification process had almost no effect on air permeability and confirmed that the Fe@UiO-66@TA/SM could potentially serve as a self-bactericidal mask that was bio-safe, and had breathability.

Conclusions

In summary, we have developed a photocatalytic Fe@UiO-66@TA/SM film on protective equipment for self-sterilization and long-term usage. Because of the unique interaction between the ferric ions and the tannic acid, UiO-66 particles were strongly co-assembled on the SM surfaces in a

simple and ultrafast way. Notably, such metal-phenolic networks (MPNs) were proved to act as a bridge for the sensibilization of the UiO-66 particles, which could enhance the potential ability to utilize the visible light region in sunlight. Additionally, the MPNs were also a typical inherent photothermal reagent which guaranteed a satisfactory thermal energy under the simulated-solar irradiation. Benefiting from the collective photocatalytic advantages, the Fe@UiO-66@TA/SM could achieve a high-efficiency self-sterilization property against both Gram-positive *S. aureus* and Gram-negative *P. aeruginosa* (more than 99%) upon the irradiation with stimulated-solar light for only 20 min. Notably, the antibiofilm experiments indicated that the Fe@UiO-66@TA/SM could conspicuously reduce and destroy biofilms. The biocompatibility results demonstrated that the Fe@UiO-66@TA/SM maintained excellent breathability, haemocompatibility and cytocompatibility, permitting the safety of the skin when it is touched. Overall, the Fe@UiO-66@TA/SM surface, we developed here, showed a methodology for the construction of a self-sterilization SM with efficient bactericidal properties and good biosafety. This strategy also offers a new hope for mitigating the pollution caused by the compulsory use of protective equipment and reduce the heavy burden on the environment.

Author contributions

Lingwan Hao: conceptualization, methodology, data analysis, writing – original draft. Jie Gao: data analysis, writing – original draft. Xiaoli Han: data curation. Zexiang Li: formal analysis. Yanhong Dong: resources. Liwei Sun: validation. Lu Zhou: software guidance. Zhaocai Ning: methodology, data analysis. Jie Zhao: resources, validation. Rujian Jiang: resources, writing – review & editing, supervision.

Conflicts of interest

There are no conflicts to declare.

Acknowledgements

The authors gratefully acknowledge the financial support from the Natural Science Foundation of Shandong Province (no. ZR2022QB040 and ZR2022QH006) and the Incubation Program of Youth Innovation of Shandong Province.

References

1 C. Weiss, M. Carriere, L. Fusco, I. Capua, J. A. Regla-Nava, M. Pasquali, A. A. Scott, F. Vitale, M. A. Unal, C. Mattevi, D. Bedognetti, A. Merkoci, E. Tasciotti, A. Yilmazer, Y. Gogotsi, F. Stellacci and L. G. Delogu, Toward Nanotechnology-Enabled Approaches against the COVID-19 Pandemic, *ACS Nano*, 2020, **14**, 6383–6406.

2 R. E. Baker, A. S. Mahmud, I. F. Miller, M. Rajeev, F. Rasambainarivo, B. L. Rice, S. Takahashi, A. J. Tatem, C. E. Wagner, L.-F. Wang, A. Wesolowski and C. J. E. Metcalf, Infectious disease in an era of global change, *Nat. Rev. Microbiol.*, 2022, **20**, 193–205.

3 Y. Yang, F. Peng, R. Wang, K. Guan, T. Jiang, G. Xu, J. Sun and C. Chang, The deadly coronaviruses: The 2003 SARS pandemic and the 2020 novel coronavirus epidemic in China, *J. Autoimmun.*, 2020, **109**, 1041.

4 D. E. Morris, D. W. Cleary and S. C. Clarke, Secondary Bacterial Infections Associated with Influenza Pandemics, *Front. Microbiol.*, 2017, **8**, 1041.

5 R. M. Jones and L. M. Brosseau, Aerosol Transmission of Infectious Disease, *J. Occup. Environ. Med.*, 2015, **57**, 501–508.

6 K. P. Fennelly, Particle sizes of infectious aerosols: implications for infection control, *Lancet Respir. Med.*, 2020, **8**, 914–924.

7 Y. Chen, J. Ao, J. Zhang, J. Gao, L. Hao, R. Jiang, Z. Zhang, Z. Liu, J. Zhao and L. Ren, Bioinspired superhydrophobic surfaces, inhibiting or promoting microbial contamination?, *Mater. Today*, 2023, **67**, 468–494.

8 R. Sommerstein, C. A. Fux, D. Vuichard-Gysin, M. Abbas, J. Marschall, C. Balmelli, N. Troillet, S. Harbarth, M. Schlegel, A. Widmer and Swissnoso, Risk of SARS-CoV-2 transmission by aerosols, the rational use of masks, and protection of healthcare workers from COVID-19, *Antimicrob. Resist. Infect. Control*, 2020, **9**, 100.

9 T. T. Le, E. J. Curry, T. Vinikoor, R. Das, Y. Liu, D. Sheets, K. T. M. Tran, C. J. Hawxhurst, J. F. Stevens, J. N. Hancock, O. R. Bilal, L. M. Shor and T. D. Nguyen, Piezoelectric Nanofiber Membrane for Reusable, Stable, and Highly Functional Face Mask Filter with Long-Term Biodegradability, *Adv. Funct. Mater.*, 2022, **32**, 2113040.

10 M. Yousefimashouf, R. Yousefimashouf, M. S. Alikhani, H. Hashemi, P. Karami, Z. Rahimi and S. M. Hosseini, Evaluation of the bacterial contamination of face masks worn by personnel in a center of COVID 19 hospitalized patients: A cross-sectional study, *New Microbes New Infect.*, 2023, **52**, 101090.

11 H. Du, S. Huang and J. Wang, Environmental risks of polymer materials from disposable face masks linked to the COVID-19 pandemic, *Sci. Total Environ.*, 2022, **815**, 152980.

12 H. P. Lee and A. K. Gaharwar, Light-Responsive Inorganic Biomaterials for Biomedical Applications, *Adv. Sci.*, 2020, **7**, 2000863.

13 D.-L. Versace, L. Breloy, E. Palierse and T. Coradin, Contributions of photochemistry to bio-based antibacterial polymer materials, *J. Mater. Chem. B*, 2021, **9**, 9624–9641.

14 Z. Liu, X. Jiang, Z. Li, Y. Zheng, J.-J. Nie, Z. Cui, Y. Liang, S. Zhu, D. Chen and S. Wu, Recent progress of photo-excited antibacterial materials via chemical vapor deposition, *Chem. Eng. J.*, 2022, **437**, 135401.

15 Z. Youssef, L. Colombeau, N. Yesmurzayeva, F. Baros, R. Vanderesse, T. Hamieh, J. Toufaily, C. Frochot, T. Roques-Carmes and S. Acherar, Dye-sensitized nano-

particles for heterogeneous photocatalysis: Cases studies with TiO_2, ZnO, fullerene and graphene for water purification, *Dyes Pigm.*, 2018, **159**, 49–71.
16 V.-N. Nguyen, Z. Zhao, B. Z. Tang and J. Yoon, Organic photosensitizers for antimicrobial phototherapy, *Chem. Soc. Rev.*, 2022, **51**, 3324–3340.
17 A. Joe, S.-H. Park, D.-J. Kim, Y.-J. Lee, K.-H. Jhee, Y. Sohn and E.-S. Jang, Antimicrobial activity of ZnO nanoplates and its Ag nanocomposites: Insight into an ROS-mediated antibacterial mechanism under UV light, *J. Solid State Chem.*, 2018, **267**, 124–133.
18 J. Wei, H. Zhao, L. Zhang, S. Chai, H. Liu, Y. Wang and J. Xue, Vis-UV Upconverting bacteriostatic hydrophobic bacterial cellulose film for personal protective masks, *Carbohydr. Polym.*, 2022, **297**, 119967.
19 S. Kumar, M. Karmacharya, S. R. Joshi, O. Gulenko, J. Park, G.-H. Kim and Y.-K. Cho, Photoactive Antiviral Face Mask with Self-Sterilization and Reusability, *Nano Lett.*, 2021, **21**, 337–343.
20 X. Wang, K. Ma, T. Goh, M. R. Mian, H. Xie, H. Mao, J. Duan, K. O. Kirlikovali, A. E. B. S. Stone, D. Ray, M. R. Wasielewski, L. Gagliardi and O. K. Farha, Photocatalytic Biocidal Coatings Featuring Zr_6Ti_4-Based Metal–Organic Frameworks, *J. Am. Chem. Soc.*, 2022, **144**, 12192–12201.
21 J. Wei, Y. Chen, H. Zhang, Z. Zhuang and Y. Yu, Hierarchically porous S-scheme CdS/UiO-66 photocatalyst for efficient 4-nitroaniline reduction, *Chin. J. Catal.*, 2021, **42**, 78–86.
22 Q. Zheng, X. Liu, Y. Zheng, K. W. K. Yeung, Z. Cui, Y. Liang, Z. Li, S. Zhu, X. Wang and S. Wu, The recent progress on metal-organic frameworks for phototherapy, *Chem. Soc. Rev.*, 2021, **50**, 5086–5125.
23 L. Hao, R. Jiang, Y. Fan, J.-N. Xu, L. Tian, J. Zhao, W. Ming and L. Ren, Formation and Antibacterial Performance of Metal–Organic Framework Films via Dopamine-Mediated Fast Assembly under Visible Light, *ACS Sustainable Chem. Eng.*, 2020, **8**, 15834–15842.
24 J. H. Cavka, S. Jakobsen, U. Olsbye, N. Guillou, C. Lamberti, S. Bordiga and K. P. Lillerud, A New Zirconium Inorganic Building Brick Forming Metal Organic Frameworks with Exceptional Stability, *J. Am. Chem. Soc.*, 2008, **130**, 13850–13851.
25 X. Zhao, X. Liu, Z. Zhang, X. Liu and W. Zhang, Facile preparation of a novel SnO_2@UiO-66/rGO hybrid with enhanced photocatalytic activity under visible light irradiation, *RSC Adv.*, 2016, **6**, 92011–92019.
26 Z. Sha and J. Wu, Enhanced visible-light photocatalytic performance of BiOBr/UiO-66(Zr) composite for dye degradation with the assistance of UiO-66, *RSC Adv.*, 2015, **5**, 39592–39600.
27 Y.-P. Yuan, L.-S. Yin, S.-W. Cao, G.-S. Xu, C.-H. Li and C. Xue, Improving photocatalytic hydrogen production of metal-organic framework UiO-66 octahedrons by dye-sensitization, *Appl. Catal., B*, 2015, **168**, 572–576.
28 B. Yu, C. He, W. Wang, Y. Ren, J. Yang, S. Guo, Y. Zheng and X. Shi, Asymmetric Wettable Composite Wound Dressing Prepared by Electrospinning with Bioinspired Micropatterning Enhances Diabetic Wound Healing, *ACS Appl. Bio Mater.*, 2020, **3**, 5383–5394.
29 D. Ma, G. Han, S. B. Peh and S. B. Chen, Water-Stable Metal-Organic Framework UiO-66 for Performance Enhancement of Forward Osmosis Membranes, *Ind. Eng. Chem. Res.*, 2017, **56**, 12773–12782.
30 R. H. Palmer, J. Liu, C.-W. Kung, I. Hod, O. K. Farha and J. T. Hupp, Electroactive Ferrocene at or near the Surface of Metal-Organic Framework UiO-66, *Langmuir*, 2018, **34**, 4707–4714.
31 J. Zhou, Z. Lin, Y. Ju, M. A. Rahim, J. J. Richardson and F. Caruso, Polyphenol-Mediated Assembly for Particle Engineering, *Acc. Chem. Res.*, 2020, **53**, 1269–1278.
32 M. Liu, R. Huang, M. Che, R. Su, W. Qi and Z. He, Tannic acid-assisted fabrication of Fe-Pd nanoparticles for stable rapid dechlorination of two organochlorides, *Chem. Eng. J.*, 2018, **352**, 716–721.
33 Y. Ji, Y. Wen, Z. Wang, S. Zhang and M. Guo, Eco-friendly fabrication of a cost-effective cellulose nanofiber-based aerogel for multifunctional applications in Cu(II) and organic pollutants removal, *J. Cleaner Prod.*, 2020, **255**, 120276.
34 J. Ding, Z. Yang, C. He, X. Tong, Y. Li, X. Niu and H. Zhang, UiO-66(Zr) coupled with Bi_2MoO_6 as photocatalyst for visible-light promoted dye degradation, *J. Colloid Interface Sci.*, 2017, **497**, 126–133.
35 S. Cakar and M. Ozacar, Fe-tannic acid complex dye as photo sensitizer for different morphological ZnO based DSSCs, *Spectrochim. Acta, Part A*, 2016, **163**, 79–88.
36 P. Hu, Z. Zhao, X. Sun, Y. Muhammad, J. Li, S. Chen, C. Pang, T. Liao and Z. Zhao, Construction of crystal defect sites in N-coordinated UiO-66 via mechanochemical *in situ* N-doping strategy for highly selective adsorption of cationic dyes, *Chem. Eng. J.*, 2019, **356**, 329–340.
37 X. Liu, N. K. Demir, Z. Wu and K. Li, Highly Water-Stable Zirconium Metal Organic Framework UiO-66 Membranes Supported on Alumina Hollow Fibers for Desalination, *J. Am. Chem. Soc.*, 2015, **137**, 6999–7002.
38 W. Li, H. Chen, J. Cai, M. Wang, X. Zhou and L. Ren, Poly (pentahydropyrimidine)-Based Hybrid Hydrogel with Synergistic Antibacterial and Pro-Angiogenic Ability for the Therapy of Diabetic Foot Ulcers, *Adv. Funct. Mater.*, 2023, **33**, 2303147.
39 J. Sun, L. Song, Y. Fan, L. Tian, S. Luan, S. Niu, L. Ren, W. Ming and J. Zhao, Synergistic Photodynamic and Photothermal Antibacterial Nanocomposite Membrane Triggered by Single NIR Light Source, *ACS Appl. Mater. Interfaces*, 2019, **11**, 26581–26589.
40 R. Bariki, D. Majhi, K. Das, A. Behera and B. G. Mishra, Facile synthesis and photocatalytic efficacy of UiO-66/$CdIn_2S_4$ nanocomposites with flowerlike 3D-microspheres towards aqueous phase decontamination of triclosan and H_2 evolution, *Appl. Catal., B*, 2020, **270**, 118882.
41 J. Wang, X. Liu, C. Li, M. Yuan, B. Zhang, J. Zhu and Y. Ma, Fabrication of perylene imide-modified NH_2-UiO-66 for

enhanced visible-light photocatalytic degradation of tetracycline, *J. Photochem. Photobiol., A*, 2020, **401**, 118882.
42 H. Liu, J. Zhang and D. Ao, Construction of heterostructured $ZnIn_2S_4$@NH_2-MIL-125(Ti) nanocomposites for visible-light-driven H_2 production, *Appl. Catal., B*, 2018, **221**, 433–442.
43 A. Sheikh, K. Soni and N. Lakshmi, Study of structural and electrochemical properties of Ilmenite ($FeTiO_3$) doped TiO_2, *Mater. Today: Proc.*, 2022, **49**, 1857–1860.
44 P. Wardman, Reduction Potentials of One–Electron Couples Involving Free Radicals in Aqueous Solution, *J. Phys. Chem. Ref. Data*, 1989, **18**, 1637–1755.
45 B. H. J. Bielski, D. E. Cabelli, R. L. Arudi and A. B. Ross, Reactivity of perhydroxyl/superoxide radicals in aqueous solution, *J. Phys. Chem. Ref. Data*, 1985, **14**, 1041–1100.
46 L. Sheng, Z. Zhang, Y. Zhang, E. Wang, B. Ma, Q. Xu, L. Ma, M. Zhang, G. Pei and J. Chang, A novel "hot spring"-mimetic hydrogel with excellent angiogenic properties for chronic wound healing, *Biomaterials*, 2021, **264**, 120414.
47 L. Hao, R. Jiang, J. Gao, J.-N. Xu, L. Tian, X. Zhang, S. Zhou, J. Zhao and L. Ren, Metal-organic framework (MOF)-based slippery liquid-infused porous surface (SLIPS) for purely physical antibacterial applications, *Appl. Mater. Today*, 2022, **27**, 101430.